eScience 3 (2023) 100096

Contents lists available at ScienceDirect

eScience

journal homepage: www.keaipublishing.com/en/journals/escience

Research Paper

Hybrid working mechanism enables highly reversible Zn electrodes

Libei Yuan [a,b], Junnan Hao [b], Bernt Johannessen [c], Chao Ye [b], Fuhua Yang [a], Chao Wu [a,*], Shi-Xue Dou [a], Hua-Kun Liu [a,*], Shi-Zhang Qiao [b,*]

[a] Institute for Superconducting and Electronic Materials, Australian Institute for Innovative Materials, University of Wollongong, Wollongong, New South Wales, 2522 Australia
[b] School of Chemical Engineering and Advanced Materials, The University of Adelaide, Adelaide, South Australia, 5005 Australia
[c] Australian Synchrotron, 800 Blackburn Rd, Clayton, VIC, 3168 Australia

HIGHLIGHTS

- New working mechanism by combining solid/electrolyte interphase (SEI) and nucleation layers is reported.
- A preferred (002) Zn deposition under SEI layer is realized for first time.
- Nafion exhibits the SEI mechanism by blocking water and providing Zn^{2+} channels.
- Boron nitride (BN) guides the Zn (002) deposition based on the epitaxial mechanism.

GRAPHICAL ABSTRACT

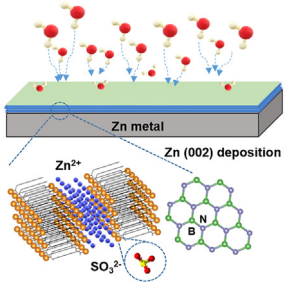

ARTICLE INFO

Keywords:
Aqueous Zn-ion batteries
Hybrid working mechanism
Boron nitride
Nafion

ABSTRACT

Zn dendrite growth and water-related side reactions have been criticized to hinder actual applications of aqueous Zn-ion batteries. To address these issues, a series of Zn interfacial modifications of building solid/electrolyte interphase (SEI) and nucleation layers have been widely proposed, however, their effectiveness remains debatable. Here, we report a boron nitride (BN)/Nafion layer on the Zn surface to efficiently solve Zn problems through combining the hybrid working mechanisms of SEI and nucleation layers. In our protective layer, Nafion exhibits the SEI mechanism by blocking water from the Zn surface and providing abundant channels for rapid Zn^{2+} transmission, whilst BN nanosheets induce Zn deposition underneath with a preferred (002) orientation. Accordingly, dendrite-free and side-reaction-free Zn electrode with (002) deposition under the protective layer is realized for the first time, as reflected by its high reversibility with average Coulombic efficiency of 99.2% for > 3000 h. The protected Zn electrode also shows excellent performance in full cells when coupling with polyaniline cathode under the strict condition of lean electrolyte addition. This work highlights insights for designing highly reversible metal electrodes towards practical applications.

1. Introduction

Aqueous batteries have attracted great attention for scalable energy storage because of their advantages in cost, safety, and environmental benignity [1]. Additionally, the insensitivity to moisture and oxygen of the aqueous electrolyte simplifies the battery assembly and lowers the requirements of the assembly environment, contributing to the efficiency of battery manufacturing [2,3]. Among aqueous batteries, Zn-ion

* Corresponding authors.
E-mail address: s.qiao@adelaide.edu.au (S.-Z. Qiao).

https://doi.org/10.1016/j.esci.2023.100096
Received 13 November 2022; Received in revised form 18 December 2022; Accepted 10 January 2023
Available online 17 January 2023

batteries (ZIBs) have shown promising potential for large-scale applications due to the direct utilization of metallic Zn electrodes [4]. Zn electrodes not only exhibit a high overpotential against H_2 evolution but also feature a high theoretical specific capacity of 820 mA h g^{-1}, which helps to broaden the working voltage window and enhance the energy density of ZIBs as well [5–7].

Although metallic Zn electrodes have shown attractive advantages, their thermodynamic stability in the water-based electrolytes and uneven Zn deposition during stripping/plating processes also bring challenges for practical applications of ZIBs, such as water-induced Zn corrosion, H_2 evolution, and Zn dendrite growth [8–10]. These side reactions and the dendritic deposition significantly reduce the reversibility of Zn electrodes, resulting in short circuits and a shortened battery lifespan [11]. Lots of efforts have been devoted to addressing these issues with a variety of strategies being proposed, such as electrolyte optimization and interfacial modifications of the Zn electrodes [12]. In terms of the electrolyte optimizations, two methods, specifically developing highly concentrated electrolytes and/or introducing other cosolvents, can suppress side reactions and dendrite growth to some extent [13,14]. However, they inevitably increase both cost and viscosity, raise safety concerns, and significantly compromise the superiority of aqueous electrolytes [15]. For the interfacial modification of Zn electrodes, two main methods of building artificial solid/electrolyte interphase (SEI) layers and/or nucleation layers, have been widely reported [16]. Generally, the artificial SEI layer needs poor electronic conductivity and high Zn^{2+} conductivity to guarantee the Zn^{2+} transportation through the layer. Meanwhile, the SEI protective layer prevents direct contact between the aqueous electrolyte and Zn electrodes to reduce water-induced H_2 evolution and Zn corrosion [17,18]. To date, a variety of organic and inorganic SEI protective layers have been proposed [19,20]. Specifically, the organic-based SEI layers feature high Zn^{2+} ionic conductivity, but such layers suffer from inferior mechanical strength, leading to unsatisfactory effects in terms of inhibiting the growth of Zn dendrites [21]. As for the inorganic SEI layers, they often exhibit poor adhesion with the Zn substrate underneath, and thus easily detach from the Zn substrate under long-term cycling, canceling the initial benefits of the SEI layer.

Unlike the interfacial SEI protection strategy, the nucleation layer works with a significantly different mechanism. It generally triggers the preferred orientation and deposition of Zn^{2+} on top of its surface through the crystal lattice matching interaction between the nucleation layer and deposited Zn [22]. Although the nucleation layer induces dendrite-free deposition on the Zn surface, the freshly deposited Zn still directly contacts the aqueous electrolyte [23]. Under the circumstances, the water-induced side reactions can continually occur both whilst the battery is in operation and idle, which compromises the effectiveness of the nucleation layers with respect to the Zn reversibility. Therefore, it is a reasonable strategy to construct a protective film that integrates the advantages of the traditional interface SEI layer and the interface nucleation layer to achieve a better Zn electrode.

Here, we report an artificial protective film composed of Nafion polymer and two-dimensional (2D) boron nitride (BN) sheets to achieve highly reversible Zn electrodes. Nafion polymer has abundant sulfonic acid side chains along the polymer backbone, which are organized in clusters with a tunnel size of ~4 nm (40 Å), which is much larger than the diameter of Zn^{2+} ion (0.74 Å). Thus, Nafion can not only block water molecules from the surface of Zn electrode but also enable the fast transfer of Zn^{2+} through the protective layer during the Zn plating/stripping processes. As an isoelectronic analog of graphene, BN has the same hexagonal structure as the Zn (002) facet, which can effectively guide the orientation of Zn deposition (crystal lattice matching) [24]. As a result, the BN/Nafion layer allows a side-reaction-free Zn electrode with dendrite-free Zn (002) deposition underneath according to the hybrid working mechanism by combining the SEI layer and the nucleation layer. This finding was evidenced by three-dimensional (3D) confocal images and scanning electron microscopy (SEM). The BN/Nafion-protected Zn electrode (denoted as BN/Nafion@Zn) delivered a high average Coulombic efficiency (CE) of 99.2% under a small current density of 1 mA cm^{-2} in Cu–Zn cells and stable plating/stripping cycling for > 3000 h in symmetric cells under 1 mA cm^{-2} and the capacity of 0.5 mA h cm^{-2}. Impressively, when the polyaniline (PANI) cathode was coupled with the BN/Nafion@Zn anode, the full cell displayed an excellent lifespan of over 2000 cycles at 5 C with a capacity retention of ~92.5%, which is much higher than the counterpart with the bare Zn electrode.

2. Results and discussion

The original process of Zn^{2+} ions plating on a Zn substrate is shown in Fig. 1a. The unprotected Zn^{2+} ions closed to the bare Zn surface are initially reduced to Zn^0, which leads to a concentration gradient of Zn^{2+} in the aqueous electrolyte. Protrusions on the surface of Zn electrode can accumulate relatively more Zn^{2+} ions during the initial plating process, as opposed to other areas of the electrode, resulting in a considerably higher electric field [25]. Consequently, these protrusions will gradually evolve into Zn nuclei and eventually form Zn dendrites upon cycling. Moreover, the active Zn electrode will react with water upon Zn plating/stripping by generating H_2 and parasitic $Zn_4SO_4(OH)_6{\cdot}xH_2O$ by-products, which seriously reduces the Zn reversibility and battery lifespan [26]. To solve these problems, our method is proposed by combining the working mechanism of the SEI and nucleation layer. Accordingly, the BN /Nafion layer was built on the surface of Zn electrode through a facile spin-coating method, in which BN was dispersed into ethyl alcohol through ultrasonic treatment to avoid serious agglomeration (details in the Supporting Information), as confirmed by SEM (Fig. S1, Supporting Information). Benefiting from hydrophilic clusters of Nafion with a tunnel size of ~4 nm (40 Å) that is much larger than the Zn^{2+} diameter of ~0.74 Å, this SEI layer provides abundant pathways for Zn^{2+} transportation, enabling the successful Zn deposition underneath the layer [27]. Importantly, BN features the same atomic structure as graphene and epitaxially matches the basal (002) plane of metallic Zn, which helps to guide the layer-by-layer Zn (002) deposition under the coating layer based on the epitaxial mechanism, as illustrated in Fig. 1b. Unlike traditional working mechanism of nucleation layer to induce the surfaced Zn (002) deposition, our deposited fresh Zn did not damage the SEI layer nor come into direct contact with water molecules. Thus, water-induced side reactions were effectively suppressed.

To confirm the successful coating of BN/Nafion, X-ray powder diffraction (XRD), Fourier-transform infrared spectroscopy (FTIR), and Raman spectroscopy analyses were carried out. XRD measurements show that Nafion has an amorphous structure, as evidenced by the broad peak in its diffraction pattern (Fig. 2a). Because of the low BN content in the BN/Nafion coating layer and the high crystallinity of Zn metal, its peak at ~27° is significantly weak in the XRD pattern of BN/Nafion@Zn. Raman and FTIR spectra of pure Zn electrode, BN, Nafion, and BN/Nafion@Zn electrode were collected in Figs. 2b and c. It is clear that the bare Zn foil has no obvious Raman peak. The protected Zn electrode, however, shows similar peaks with pure BN and Nafion, indicating the presence of both materials, which was further confirmed by FTIR. Unlike the pure Zn electrode, this artificial BN/Nafion SEI coated Zn electrode exhibits several peaks. These peaks at 1060 cm^{-1}, 1145 cm^{-1}, 1201 cm^{-1}, and 976 cm^{-1} are attributed to the symmetric S–O stretching, symmetric C–F stretching, asymmetric C–F stretching, and the C–O–C stretching of the Nafion, respectively, as shown in Fig. 2c. While, the absorption peaks at ~1129 cm^{-1} and 1726 cm^{-1} correspond to the C=O and C–H stretching vibration of Nafion, respectively [28]. Small peaks at 632 cm^{-1} and 512 cm^{-1} are assigned to the stretching of C–S groups and symmetric O–S–O bending of Nafion, respectively. In addition, the peak respectively located at 798 cm^{-1} and 1352 cm^{-1} is attributed to the B–N–B out-of-plane bending vibration and the in-plane B–N stretching vibration [24].

The physical properties of the BN/Nafion coating layer were studied, and its feasibility for enhancing the Zn stability was proven. The

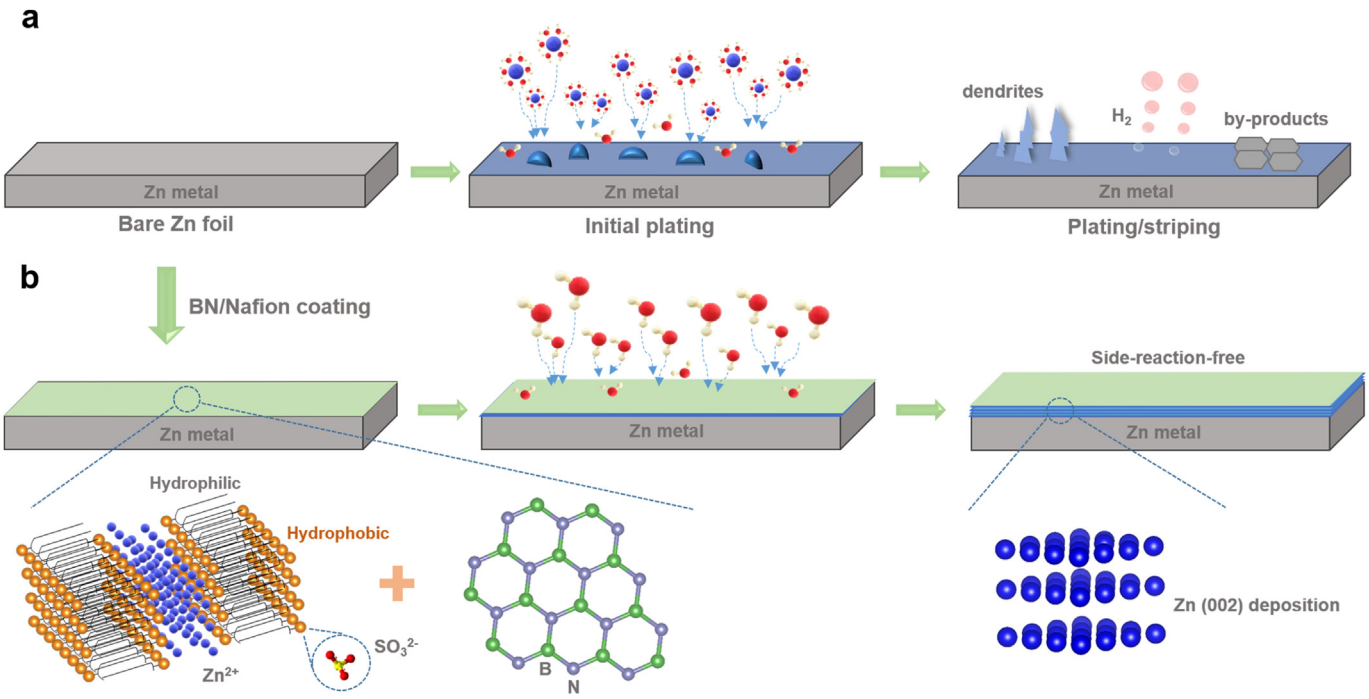

Fig. 1. Schematic illustration of the morphology evolution upon the Zn plating/stripping process of bare Zn–Zn cell (a) and BN/Nafion@Zn–BN/Nafion@Zn cell (b). The bare Zn electrode suffers from dendrite growth, water-induced H_2 evolution, and the accumulation of $Zn_4SO_4(OH)_6{\cdot}xH_2O$ by-product. In comparison, with the hybrid BN/Nafion protection, the dendrite-free Zn (002) deposition can be obtained without side reactions.

thickness of the BN/Nafion coating was established through SEM with energy dispersive spectroscopy (EDS) mapping. After the spin-coating, the Zn electrode was successfully coated by a uniform and dense BN/Nafion layer with a thickness of ~0.5 μm (Fig. 2d), which was evidenced by EDS mapping of Zn, F, and O elements (Fig. S2). The hydrophilicity of the BN/Nafion layer was evaluated in the electrolyte *via* studying the contact angle of bare Zn and BN/Nafion coated Zn electrodes, as presented in Figs. 2e and f.

Results show that the bare Zn has a large contact angle of ~85.8° with the electrolyte, indicating its poor hydrophilicity in the aqueous media. Whereas, the contact angle of BN/Nafion@Zn electrode reduces to only 31.5°, which demonstrates that the BN/Nafion artificial layer dramatically improves the hydrophilicity. This is mainly because of the rich polar functional groups of Nafion [29]. Importantly, the enhanced hydrophilicity of Zn electrode thermodynamically reduces its free energy towards the aqueous electrolyte, which contributes to the homogeneous nucleation formation. The corrosion resistance of Zn electrodes with/without BN/Nafion protection in the aqueous electrolyte was evaluated by linear sweep voltammetry (LSV, Fig. 2g). The bare Zn has a corrosion potential of −1.02 V, whilst the potential of BN/Nafion@Zn moves to −0.99 V, elucidating the enhanced corrosion resistance [30].

The effectiveness of BN/Nafion protection on the suppression of H_2 evolution and by-product formation was studied. Fig. 2h shows LSV curves of Zn electrodes with/out BN/Nafion protection in Zn^{2+}-free electrolyte of 2 M Na_2SO_4. Results revealed that the H_2 evolution potential moves from −1.62 V to −2.01 V with BN/Nafion protection, indicating effective suppression of H_2 evolution by the BN/Nafion coating [31]. To evaluate the by-product generation of water-induced corrosion reaction, both Zn electrodes with/without protection were immersed in 2 M $ZnSO_4$ electrolyte for 10 days, and their morphology was studied by 3D laser confocal scanning microscopy (Fig. S3). The bare Zn electrode surface is severely corroded after soaking for 10 days, as evidenced by its uneven surface morphology. With the protection of BN/Nafion, the Zn electrode still exhibits an even surface, indicating suppression of corrosive reactions [32]. Fig. 2i compares the XRD patterns of both soaked electrodes. In the case of the bare Zn foil, its pattern shows strong peaks at 8.9° and 16.5° that belong to $Zn_4SO_4(OH)_6{\cdot}xH_2O$ by-product, which confirms the severe corrosion of bare Zn electrodes. The BN/Nafion@Zn foil only shows the peaks of Zn metal without any $Zn_4SO_4(OH)_6{\cdot}xH_2O$ peaks after immersion in electrolyte for 10 days, indicating that the corrosion reactions were inhibited due to the BN/Nafion coating.

The electronic resistance and Zn^{2+} conductivity are vital parameters for the artificial layer to protect Zn electrodes. Thus, these measurements on the BN/Nafion layer were carried out. As presented in Fig. S4, the electrical resistivity was tested to be ~8.8×10^5 Ω cm (the conductivity of σ is ~1.25×10^{-6} S cm^{-1}, the detail information can be found in Supporting information), demonstrating that the BN/Nafion layer is electronically insulating. Meanwhile, the ionic conductivity of the BN/Nafion based on the $ZnSO_4$ electrolyte was also investigated (Fig. S5), which shows the high Zn^{2+} conductivity of ~2.17×10^{-5} S cm^{-1}. Due to the high electronic resistance and high Zn^{2+} conductivity of the insulating BN/Nafion layer, the high potential gradient could drive the rapid Zn^{2+} diffusion through the BN/Nafion layer [33]. To quantitatively describe the diffusion of Zn^{2+} in the BN/Nafion layer, Zn^{2+} transference ($t_{Zn^{2+}}$) was further calculated. In the symmetric cell with bare Zn, $t_{Zn^{2+}}$ was obtained to be 0.32 (Fig. S6a), which is similar to previous reports [34]. After introducing the BN/Nafion layer, $t_{Zn^{2+}}$ was improved to 0.61 (Fig. S6b). This is because rich O-containing groups in Nafion provide active sites for Zn^{2+} transfer. And the dense BN/Nafion layer also blocks the solvated water and SO_4^{2-} from diffusing through it.

The function of the BN/Nafion protective layer in enhancing the Zn stability was evaluated through repeated plating/stripping measurements by testing symmetrical Zn cells at 0.5 mA cm^{-2}. It can be found from Fig. 3a that the bare Zn–Zn symmetrical cell fails after cycling for approximately 260 h because of the internal short-circuit. The BN/Nafion@Zn-based symmetrical cell, however, displays a much longer cycling life of over 3000 h without short-circuit benefiting from the dendrite-free Zn deposition. After increasing the high current density of 5 mA cm^{-2} and large capacity of 5 mA h cm^{-2}, the bare Zn cell shows a battery failure after cycling for only ~40 h (Fig. S7). In contrast, the symmetrical Zn cell with the BN/Nafion protection displays good cycling

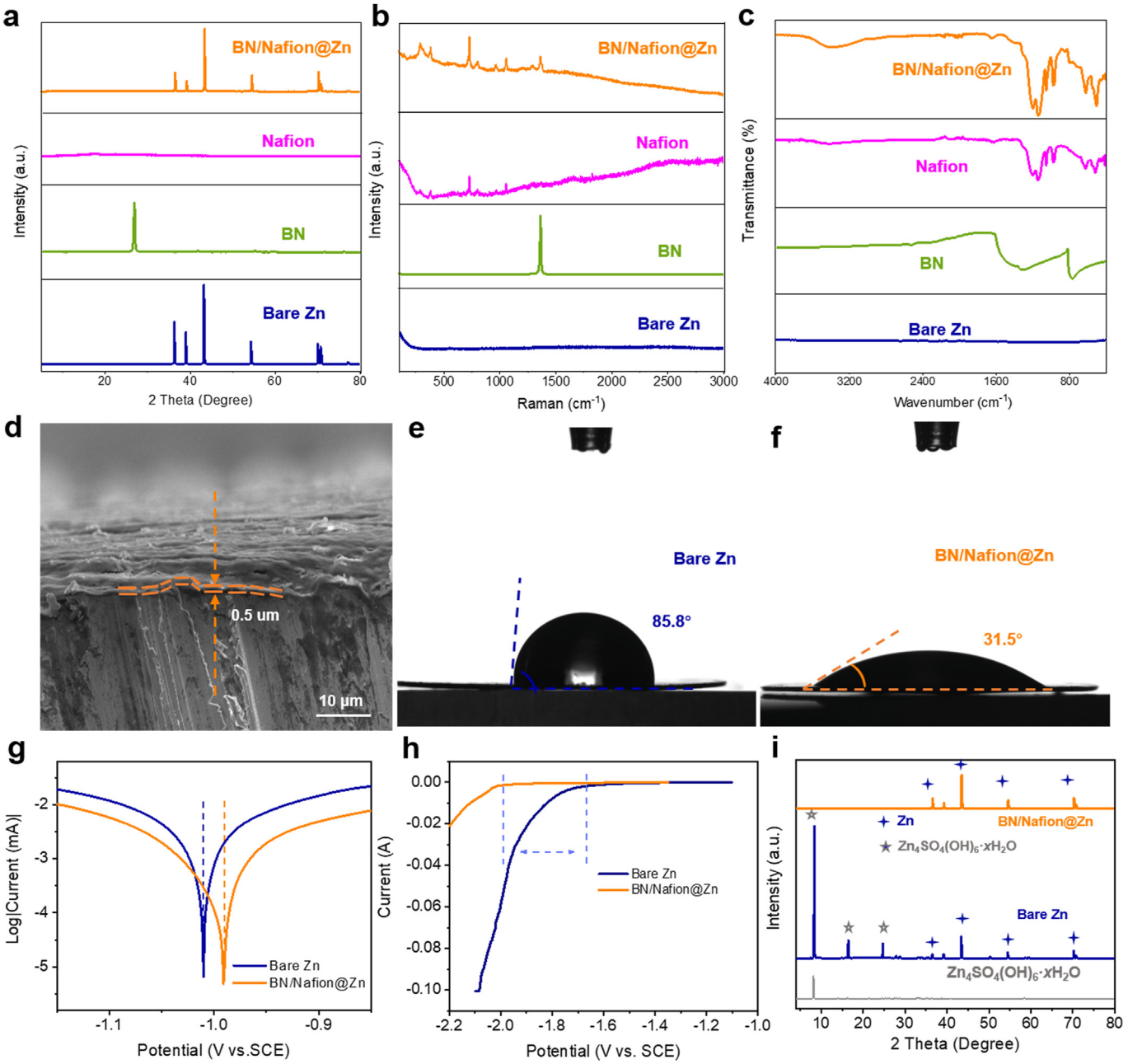

Fig. 2. The Zn electrode characterization with the BN/Nafion protection. (a) XRD patterns of bare Zn, BN, Nafion, and BN/Nafion@Zn. (b) Raman spectra and (c) FTIR spectra of four samples. (d) Cross-sectional SEM image of BN/Nafion@Zn electrode. Contact angle measurements in aqueous media of (e) bare Zn and (f) BN/Nafion@Zn. (g) Linear polarization curves showing the corrosion of bare Zn and BN/Nafion@Zn. (h) LSV response curves for different electrodes in the Zn^{2+}-free electrolyte at 0.1 mV s^{-1}. (i) XRD patterns of both bare Zn and BN/Nafion@Zn electrodes after soaking for 10 days in electrolyte.

stability. There is no battery failure or significant voltage fluctuation found even after cycling for 320 h, indicating the effectiveness of BN/Nafion protection under the high current density. The battery rate performance was further studied under the increased current densities from 0.5 mA cm^{-2} to 20 mA cm^{-2} (Fig. 3b). Compared to the BN/Nafion@Zn cell, the bare Zn cell consistently exhibits higher voltage hysteresis. The low polarization and favorable stability confirm the benefits of the BN/Nafion layer to promote the Zn stripping/plating. The CE of Zn stripping/plating is one of the most vital parameters for effectively evaluating Zn reversibility. For the Cu–Zn half cell, it displays a low initial CE of only ~77.5%, and the CE gradually increases in the following cycles with an average value of ~97.8% (Fig. 3c). Such low CE indexed to the poor Zn reversibility is mainly caused by dendrite growth and side reactions. Moreover, the CE value fluctuates after ~170 cycles, which demonstrates the failure of the battery. In comparison, the Cu–BN/Nafion@Zn cell shows an initial CE of ~88.5% and a higher average value of ~99.2% after 1200 cycles. This mainly benefits from the suppression of dendrite formation and side reactions. To clearly see the extent of Zn corrosion, Zn electrodes after the 200th cycle were stripped out of the Cu–Zn cells for XRD measurements, as shown in Fig. 3d. The bare Zn electrode shows a significant peak at ~9.8°, indexed to the (002) plane of $Zn_4SO_4(OH)_6{\cdot}xH_2O$, which confirms the significant corrosion during battery cycling. For the protected Zn electrode, however, the peak at ~9.8° is barely discernible, indicating that Zn electrode corrosion was significantly suppressed [35]. The ratio of the diffraction intensity of the (002) planes to that of the (101) planes, $I_{(002)}/I_{(101)}$, (the diffraction intensity ratio) can reflect the preferred growth direction of Zn deposition. The obtained $I_{(002)}/I_{(101)}$ ratio of the BN/Nafion@Zn electrode is ~2.1,

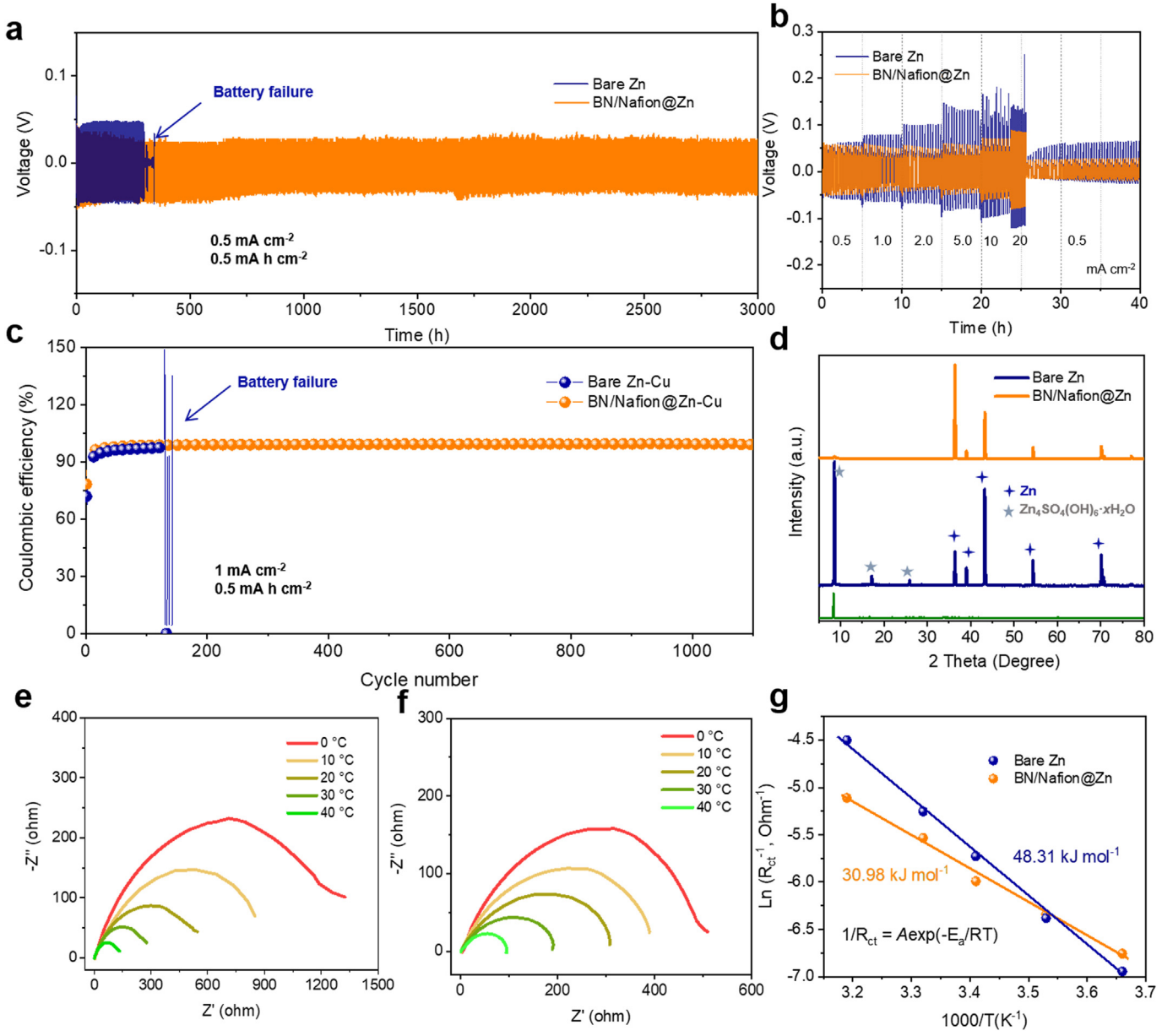

Fig. 3. The Zn reversibility studies. (a) Cycling stability of the symmetrical cells with bare Zn and the BN/Nafion@Zn electrode at 0.5 mA cm^{-2}, respectively. (b) Rate capacity of both cells under current densities from 0.5 to 20 mA cm^{-1}. (c) CEs of Cu–Zn and Cu–BN/Nafion@Zn cells under 1 mA cm^{-2}. (d) XRD patterns of bare Zn and BN/Nafion@Zn electrodes after the 200th cycling. EIS spectra collected at various temperatures for (e) bare symmetric Zn cell and (f) BN/Nafion@Zn cell. (g) Arrhenius curves fitted from the series of R_{ct} obtained at different temperatures.

which is much higher than that of the bare Zn electrode (0.34) [36]. This demonstrates that the BN/Nafion@Zn electrode features preferential Zn^{2+} deposition parallel to the (002) crystal planes. The activation energy (E_a) for the de-solvation of Zn^{2+} can be obtained based on the Arrhenius Equation (Equation (1)), which can be employed to study the Zn deposition kinetics

$$\frac{1}{R_{ct}} = Ae^{-\frac{E_a}{RT}} \quad (1)$$

Where R_{ct}, A, E_a, R, and T are interfacial resistance, frequency factor, gas constant, and absolute temperature, respectively [37]. E_a can be simulated by Nyquist plots and measured in symmetric cells at various temperatures from 0 to 40 °C (Figs. 3e–g). E_a of BN/Nafion@Zn electrode was measured to be 30.98 kJ mol^{-1}, smaller than that of bare Zn (48.31 kJ mol^{-1}), further indicating promotion of the de-solvation effect and acceleration of the Zn deposition kinetics of the BN/Nafion layer [38].

To intrinsically study the feasibility of BN/Nafion layer in protecting Zn electrodes, 3D laser confocal scanning microscopy and SEM of Zn electrodes with/without BN/Nafion protection were carried out after 100 cycles in symmetrical cells. The 3D confocal image shows that serious corrosion has occurred at the edges and the surface of bare Zn electrode (Fig. 4a). After increasing the cycle number to 150 and 200 cycles, the Zn corrosion was aggravated, as evidenced by the by-product accumulation (Figs. 4b and c). In comparison, the BN/Nafion@Zn electrode shows a smooth surface even after 200 cycles (Figs. 4d–f), demonstrating suppression of side reactions by the BN/Nafion layer. More detailed information about the surfaces of the cycled Zn was presented in SEM images. It can be observed that the Zn plating on the bare Zn electrode is dendritic, loose, and porous (Fig. 4g), which significantly impacts the Zn reversibility for plating/stripping. The Zn electrode surface would be damaged after repeated cycling (Figs. 4h and i). In strong contrast, the Zn plating/stripping on the surface of BN/Nafion@Zn

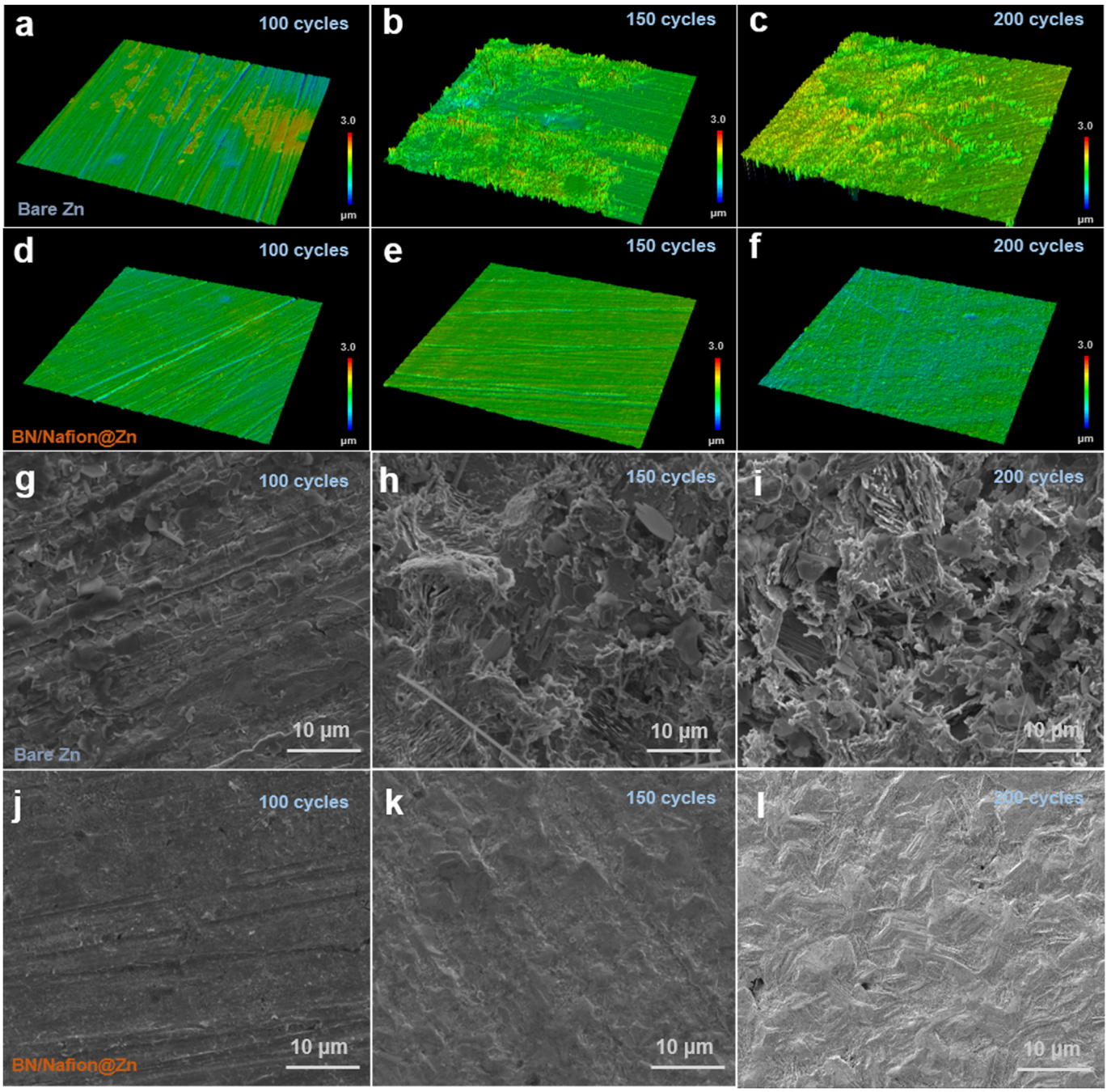

Fig. 4. The Zn plating behavior. 3D confocal images of bare Zn electrode (a–c) and BN/Nafion@Zn electrode after 100 to 200 cycles (d–f). SEM images of bare Zn electrode (g–i) and BN/Nafion@Zn electrode after different cycles (j–l).

electrode is compact, dense, and homogeneous (Figs. 4j–l). As proved by the XRD pattern, the uniform (002) deposition contributes to the high reversibility of the Zn chemistry [39]. After the ultrasonic cleaning, the cross-sectional image further confirmed uniform Zn deposition without dendrite formation (Fig. S8a). The EDS map of Zn element shows the layer-by-layer Zn deposition, demonstrating that the BN/Nafion layer contributes to dendrite-free (002) Zn deposition (Fig. S8b) [40].

In addition to dendrite studies, it is of vital importance to study H_2 evolution during battery operation, since H_2 evolution reaction is one of the most significant hazards for aqueous ZIBs. Fig. 5a shows the *in-situ* gas chromatography (GC) tests conducted upon the Zn plating/stripping process under a current density of 5.0 mA cm^{-2}. It can be found that the H_2 evolution occurs simultaneously with Zn plating. The intensity of H_2 evolution is ~172 ppm at the beginning of Zn plating in the bare Zn cell (Fig. S9). Although the H_2 evolution decreases to some extent during the following plating/stripping processes, it still maintains a high value of ~105 ppm after plating/stripping for 3.5 h. This significant H_2 evolution was also confirmed by the cycled Zn symmetric cell, which shows serious swelling of the cell after 500 cycles (Fig. S10). After coating the Zn with a protective BN/Nafion layer, the intensity of H_2 evolution is effectively suppressed, as shown in Fig. 5b. Fig. S11 summarizes the specific amount of H_2 evolution, which maintains a low value of ~46 ppm during the entire process of Zn plating/stripping. These findings reveal the effectiveness of the BN/Nafion layer in inhibiting water-induced H_2 evolution during battery operation. To understand the BN/Nafion function towards guiding Zn (002) deposition in depth, the density functional theory (DFT)

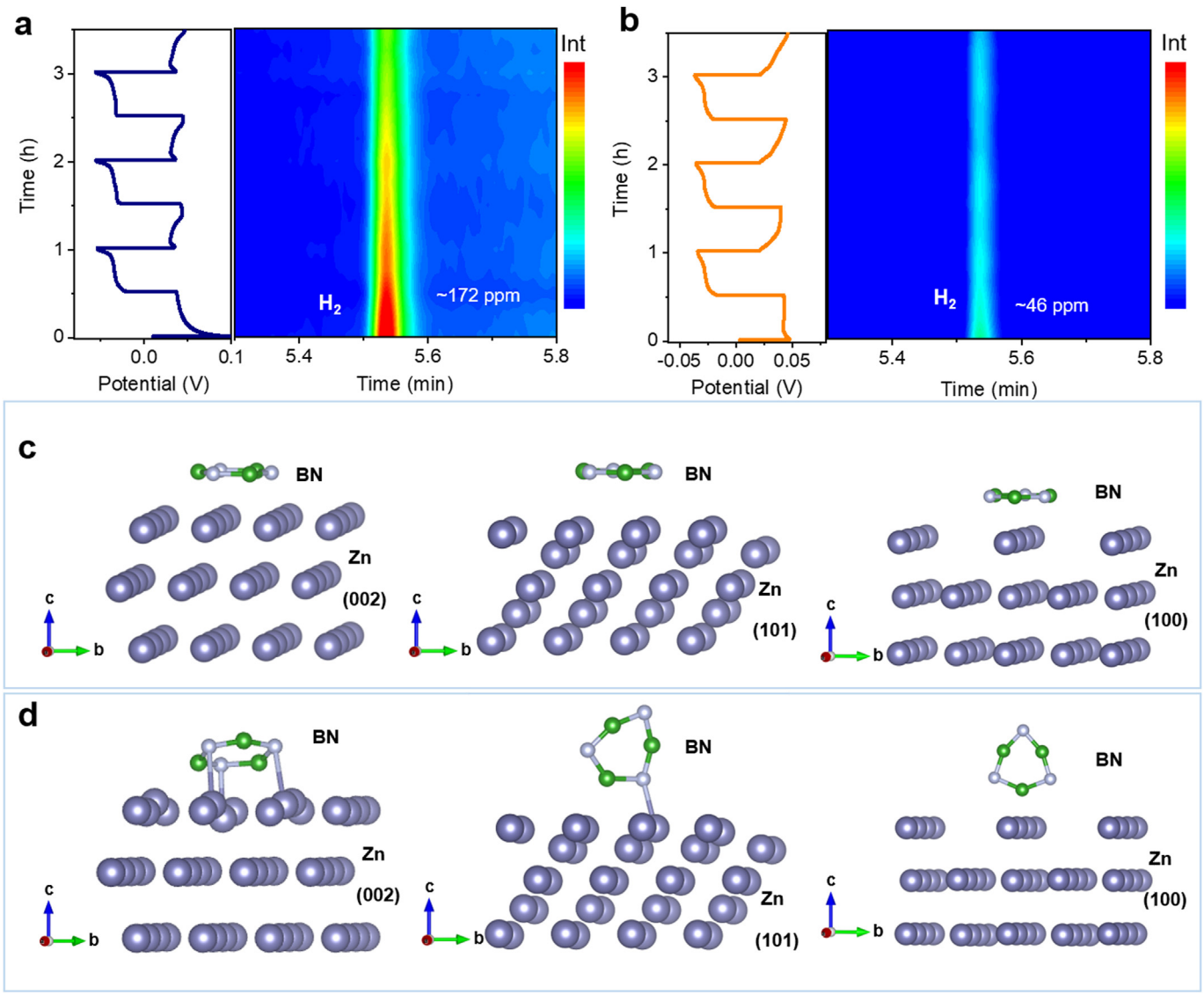

Fig. 5. The Zn reversibility studies during battery operation. *In-situ* GC measurements to assess H_2 evolution in symmetrical cells with/without BN/Nafion layer. DFT calculations of interactions of the BN molecule with different Zn lattice planes, including (002), (101), and (100) planes (c) and geometrical structures after the structure optimization (d).

simulation was carried out. Fig. 5c presents models of the BN molecule with different Zn lattice planes at the interphase, including Zn (002), Zn (101), and Zn (100) [41]. Fig. 5d summarizes the geometrical structures after the structure optimization. After repeated simulations, only the Zn (002) facet can come into close contact with the BN molecule, which is mainly due to their highly matched hexagonal structures [42]. Benefiting from the same hexagonal structure, the BN in the protective layer contributes to the layer-by-layer Zn (002) deposition.

The function of the BN/Nafion layer in the Zn full cell was assessed in PANI−Zn batteries. The PANI cathode was obtained through liquid-phase synthesis, and its morphology was studied after freeze drying (Fig. S12). SEM images show that PANI features a porous 3D network structure, which facilitates the infiltration of electrolyte as well as the diffusion of ions [43–45]. The galvanostatic discharge-charge curves under a low current density of 1 A g^{-1} were collected for the full cells of PANI−Zn with/without BN/Nafion, as illustrated in Fig. 6a. Compared to the full cell with the bare Zn electrode, the cell with BN/Nafion@Zn electrode shows a distinct and long second plateau, demonstrating the larger storage amount of Zn^{2+} [46,47]. Accordingly, the discharge capacity of the cell with BN/Nafion@Zn electrode increases from ~175.2 to ~195.1 mA h g^{-1}. In addition, the cycling stability of both coin cells with bare Zn electrode and BN/Nafion@Zn electrode was then tested at a higher current density of 5 A g^{-1}, in which the added electrolyte amount (30 μL) was controlled to only infiltrate the separator of glass fiber. As presented in Fig. 6b, the coin cell with bare Zn electrode exhibits a rapid capacity fading in the initial 200 cycles with a low capacity retention of ~41.5% after 2000 cycles. While, the superior cycling stability in the PANI−BN/Nafion@Zn cell is pronounced. A capacity of ~86.3 mA h g^{-1} remains after 2000 cycles, which equates to the capacity retention of ~95.8%. SEM images were collected to compare the morphology of cycled Zn electrodes in Fig. S13. The bare Zn electrode shows serious corrosion and significant by-product accumulation after 500 cycles. Meanwhile, the corrosion and by-product formation on the BN/Nafion@Zn is suppressed, which contributes to the high Zn reversibility.

By replacing the small-capacity coin cell, the PANI−BN/Nafion@Zn pouch cells were further assembled and tested under strict conditions with the lean electrolyte addition of 2 μL mg^{-1} (Fig. S14). Because the lean electrolyte study is helpful for the real battery performance evolution, which is also one of the most vital steps to actually realize battery commercialization [48]. Under a low current of 50 mA, the

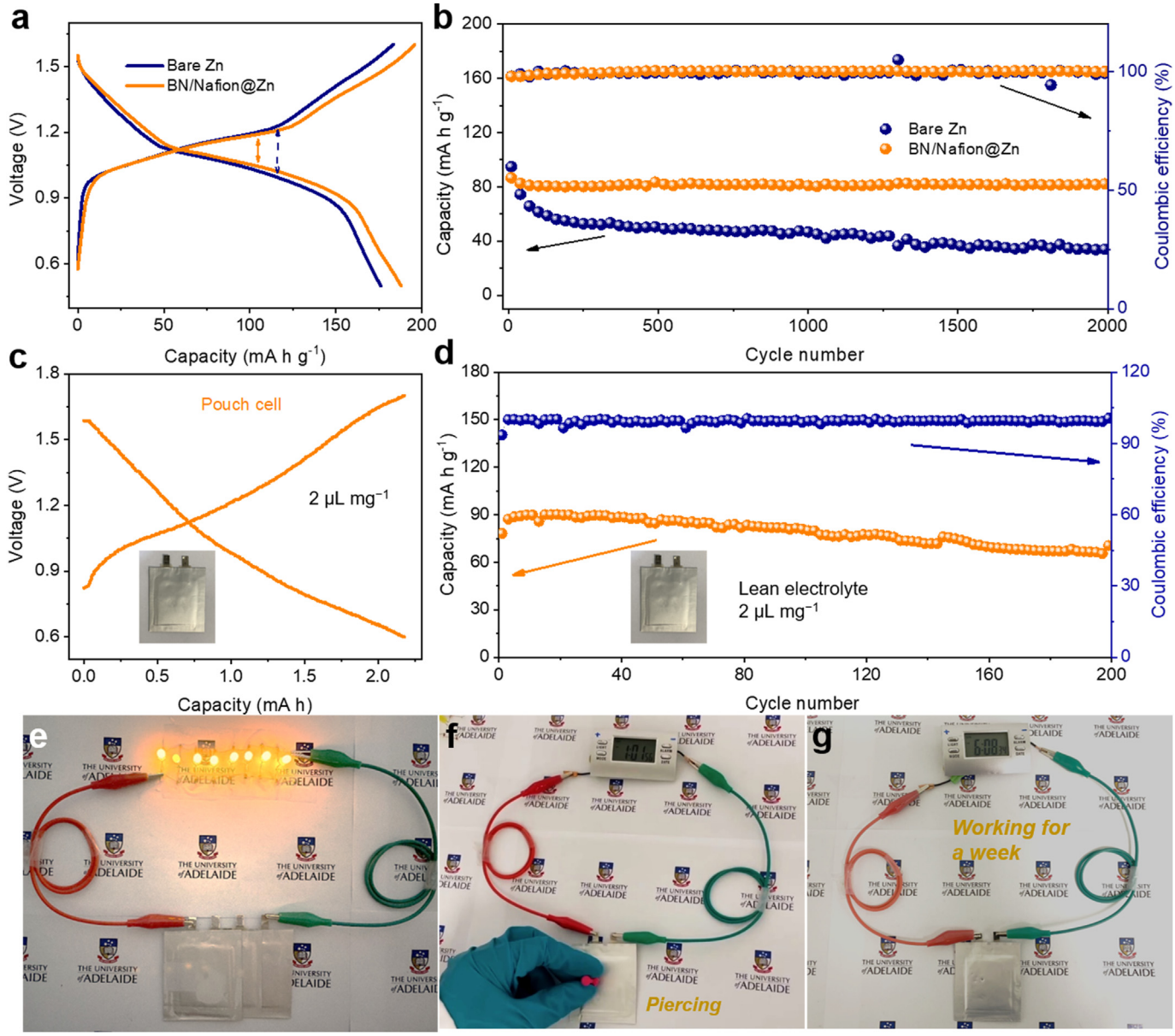

Fig. 6. Full-cell performance characterization. (a) Galvanostatic charge-discharge curves of PANI−Zn coin cells with/without BN/Nafion layer at 1 A g^{-1}. (b) Cycling performance of PANI−Zn coin cells with/without BN/Nafion layer at 5 A g^{-1}. (c) Charge-discharge curves for PANI−Zn pouch cells at 50 mA, in which the lean electrolyte of 2 μL mg^{-1} was added. (d) Cycling performance of PANI−Zn pouch cells at 80 mA. The practical evaluation of PANI−Zn pouch cells: (e) by illuminating eight LEDs, (f) by powering an alarm clock after battery piercing and (g) after a whole week, indicating its superior safety.

BN/Nafion@Zn-based pouch cell displays similar charge-discharge curves to those for the counterpart in the coin cell, which indicates the electrochemical performance uniformity of the battery after scaling up in a large cell (Fig. 6c). Moreover, this pouch cell with the single layer electrode showed a high reversible capacity of 2.2 mA h. The cycling performance of BN/Nafion@Zn-based pouch cell at a high current of 80 mA was also measured in Fig. 6d. The result indicates that the cell shows outstanding reversibility with the CE of ~100%. After 200 cycles, the capacity remained at ~86.2% of its initial value. This cycling performance is also much better than those previous PANI−Zn pouch cells [32], demonstrating the strong ability of BN/Nafion layer to guarantee an excellent battery lifespan. The practicability and safety performance of this pouch cell was confirmed by powering different devices under harsh conditions. As shown in Fig. 6e, three small pouch cells in series could illuminate eight light-emitting diodes (LEDs). A single pouch cell can also power other devices, such as an alarm clock (Fig. 6f). Importantly, the cell could still power the alarm clock for a whole week after piercing the cell (Fig. 6g and Fig. S15), indicating its advantage of high safety.

3. Conclusion

In this contribution, a hybrid working mechanism for the Zn electrode modification was realized through coating a BN/Nafion layer on the surface of Zn, which not only guides the traditional Zn (002) deposition underneath but also successfully prevents contact between the water in the electrolyte and fresh Zn. Benefiting from the hydrophilic clusters with a tunnel size of 40 Å, Nafion provided abundant pathways for Zn^{2+} transportation, which guarantees the successful Zn deposition underneath the layer. Meanwhile, BN epitaxially matched the basal (002) plane of metallic Zn, which triggers layer-by-layer Zn deposition under the coating layer. In addition, H_2 evolution and the corrosion reaction during battery cycling were also effectively suppressed owing to the BN/Nafion coating, resulting in the high reversibility of Zn electrodes. As a result,

the BN/Nafion@Zn electrode showed a high average CE of 99.2% in the Cu−Zn cell under a low current density of 1 mA cm^{-2} and an extra-long cycling life of over 3000 h in the symmetrical Zn cell. When coupled with a PANI cathode, the BN/Nafion@Zn-based coin cell displayed excellent cycling stability with a capacity retention of 95.8% after 2000 cycles. After scaling up into a pouch cell, our BN/Nafion@Zn-based battery still featured a long lifespan of 200 cycles under the strict condition of lean electrolyte addition. This work provides new insights to guide layer-by-layer (002) Zn deposition underneath the SEI, which lays a solid foundation for the development of highly reversible Zn batteries.

Declaration of competing interest

The authors declare that they have no known competing financial interests or personal relationships that could have appeared to influence the work reported in this paper.

Acknowledgements

L.Y. and J.H. contributed equally to this work. The authors gratefully acknowledged the financial support from the Australian Research Council (ARC) (DP220102596, DP200100365, DE230100471, and FL170100154). DFT computations in this work were undertaken with the assistance of resources and services from the National Computational Infrastructure (NCI) and Phoenix High Performance Computing, which are supported by both Australian Government and the University of Adelaide. The authors thank Dr. Tania Silver for her critical reading of this manuscript as well.

Appendix A. Supplementary data

Supplementary data to this article can be found online at https://doi.org/10.1016/j.esci.2023.100096.

References

[1] N. Zhang, X. Chen, M. Yu, Z. Niu, F. Cheng, J. Chen, Materials chemistry for rechargeable zinc-ion batteries, Chem. Soc. Rev. 49 (2020) 4203–4219.
[2] N. Zhang, S. Huang, Z. Yuan, J. Zhu, Z. Zhao, Z. Niu, Direct self-assembly of MXene on Zn anodes for dendrite-free aqueous zinc-ion batteries, Angew. Chem. Int. Ed. 60 (2021) 2861–2865.
[3] Z. Liu, Y. Huang, Y. Huang, Q. Yang, X. Li, Z. Huang, C. Zhi, Voltage issue of aqueous rechargeable metal-ion batteries, Chem. Soc. Rev. 49 (2020) 180–232.
[4] Q. Zhao, W. Huang, Z. Luo, L. Liu, Y. Lu, Y. Li, L. Li, J. Hu, H. Ma, J. Chen, High-capacity aqueous zinc batteries using sustainable quinone electrodes, Sci. Adv. 4 (2018) eaao1761.
[5] Z. Hou, T. Zhang, X. Liu, Z. Xu, J. Liu, W. Zhou, Y. Qian, H. Fan, D. Chao, D. Zhao, A solid-to-solid metallic conversion electrochemistry toward 91% zinc utilization for sustainable aqueous batteries, Sci. Adv. 8 (2022) eabp8960.
[6] M. Chuai, J. Yang, M. Wang, Y. Yuan, Z. Liu, Y. Xu, Y. Yin, J. Sun, X. Zheng, N. Chen, High-performance Zn battery with transition metal ions co-regulated electrolytic MnO_2, eScience 1 (2021) 178–185.
[7] M. Wang, Y. Meng, K. Li, T. Ahmad, N. Chen, Y. Xu, J. Sun, M. Chuai, X. Zheng, Y. Yuan, C. Shen, Z. Zhang, W. Chen, Toward dendrite-free and anti-corrosion Zn anodes by regulating a bismuth-based energizer, eScience 2 (2022) 509–517.
[8] S. Zhang, J. Hao, H. Li, P.F. Zhang, Z.W. Yin, Y.Y. Li, B. Zhang, Z. Lin, S.Z. Qiao, Polyiodide confinement by starch enables shuttle-free Zn–iodine batteries, Adv. Mater. 34 (2022) 2201716.
[9] K. Miyazaki, Y.S. Lee, T. Fukutsuka, T. Abe, Suppression of dendrite formation of zinc electrodes by the modification of anion-exchange ionomer, Electrochemistry 80 (2012) 725–727.
[10] J.F. Parker, C.N. Chervin, E.S. Nelson, D.R. Rolison, J.W. Long, Wiring zinc in three dimensions re-writes battery performance—dendrite-free cycling, Energy Environ. Sci. 7 (2014) 1117–1124.
[11] J. Hao, L. Yuan, Y. Zhu, M. Jaroniec, S.Z. Qiao, Triple-function electrolyte regulation towards advanced aqueous Zn-ion batteries, Adv. Mater. 34 (2022) 2206963.
[12] C. Li, X. Xie, H. Liu, P. Wang, C. Deng, B. Lu, J. Zhou, S. Liang, Integrated 'all-in-one' strategy to stabilize zinc anodes for high-performance zinc-ion batteries, Natl. Sci. Rev. 9 (2022) nwab177.
[13] S. Zhang, J. Hao, D. Luo, P.F. Zhang, B. Zhang, K. Davey, Z. Lin, S.Z. Qiao, Dual-function electrolyte additive for highly reversible Zn anode, Adv. Energy Mater. 11 (2021) 2102010.
[14] Y. Zhang, M. Zhu, K. Wu, F. Yu, G. Wang, G. Xu, M. Wu, H.-K. Liu, S.-X. Dou, C. Wu, An in-depth insight of a highly reversible and dendrite-free Zn metal anode in an hybrid electrolyte, J. Mater. Chem. A 9 (2021) 4253–4261.
[15] J. Hao, J. Long, B. Li, X. Li, S. Zhang, F. Yang, X. Zeng, Z. Yang, W.K. Pang, Z. Guo, Toward high-performance hybrid Zn-based batteries via deeply understanding their mechanism and using electrolyte additive, Adv. Funct. Mater. 29 (2019) 1903605.
[16] Y. Zhang, G. Wang, F. Yu, G. Xu, Z. Li, M. Zhu, Z. Yue, M. Wu, H.-K. Liu, S.-X. Dou, Highly reversible and dendrite-free Zn electrodeposition enabled by a thin metallic interfacial layer in aqueous batteries, Chem. Eng. J. 416 (2021) 128062.
[17] H. Li, C. Guo, T. Zhang, P. Xue, R. Zhao, W. Zhou, W. Li, A. Elzatahry, D. Zhao, D. Chao, Hierarchical confinement effect with zincophilic and spatial traps stabilized zn-based aqueous battery, Nano Lett. 22 (2022) 4223–4231.
[18] Z. Cao, P. Zhuang, X. Zhang, M. Ye, J. Shen, P.M. Ajayan, Strategies for dendrite-free anode in aqueous rechargeable zinc ion batteries, Adv. Energy Mater. 10 (2020) 2001599.
[19] L.E. Blanc, D. Kundu, L.F. Nazar, Scientific challenges for the implementation of Zn-ion batteries, Joule 4 (2020) 771–799.
[20] H. Jia, Z. Wang, B. Tawiah, Y. Wang, C.-Y. Chan, B. Fei, F. Pan, Recent advances in zinc anodes for high-performance aqueous Zn-ion batteries, Nano Energy 70 (2020) 104523.
[21] L. Yuan, J. Hao, C.-C. Kao, C. Wu, H. Liu, S.X. Dou, S. Qiao, Regulation methods for the Zn/electrolyte interphase and the effectiveness evaluation in aqueous Zn-ion batteries, Energy Environ. Sci. 14 (2021) 5669–5689.
[22] J. Zheng, Q. Zhao, T. Tang, J. Yin, C.D. Quilty, G.D. Renderos, X. Liu, Y. Deng, L. Wang, D.C. Bock, Reversible epitaxial electrodeposition of metals in battery anodes, Science 366 (2019) 645–648.
[23] J. Zheng, J. Yin, D. Zhang, G. Li, D.C. Bock, T. Tang, Q. Zhao, X. Liu, A. Warren, Y. Deng, Spontaneous and field-induced crystallographic reorientation of metal electrodeposits at battery anodes, Sci. Adv. 6 (2020) eabb1122.
[24] W. Zhang, Q. Zhao, Y. Hou, Z. Shen, L. Fan, S. Zhou, Y. Lu, L.A. Archer, Dynamic interphase–mediated assembly for deep cycling metal batteries, Sci. Adv. 7 (2021) eabl3752.
[25] Y. Song, P. Ruan, C. Mao, Y. Chang, L. Wang, L. Dai, P. Zhou, B. Lu, J. Zhou, Z. He, Metal-organic frameworks functionalized separators for robust aqueous zinc-ion batteries, Micro & Nano Lett. 14 (2022) 218.
[26] H. Li, C. Guo, T. Zhang, P. Xue, R. Zhao, W. Zhou, W. Li, A. Elzatahry, D. Zhao, D. Chao, Hierarchical confinement effect with zincophilic and spatial traps stabilized Zn-based aqueous battery, Nano Lett. 22 (2022) 4223–4231.
[27] K.A. Mauritz, R.B. Moore, State of understanding of nafion, Chem. Rev. 104 (2004) 4535–4586.
[28] H. Chen, J. Liu, W. Cao, H. He, X. Li, C. Zhang, 3D printing CO_2-activated carbon nanotubes host to promote sulfur loading for high areal capacity lithium-sulfur batteries, Nano Res. (2022), https://doi.org/10.1007/s12274-022-4741-4.
[29] G. Liang, F. Mo, Q. Yang, Z. Huang, X. Li, D. Wang, Z. Liu, H. Li, Q. Zhang, C. Zhi, Commencing an acidic battery based on a copper anode with ultrafast proton-regulated kinetics and superior dendrite-free property, Adv. Mater. 31 (2019) 1905873.
[30] J. Abdulla, J. Cao, D. Zhang, X. Zhang, C. Sriprachuabwong, S. Kheawhom, P. Wangyao, J. Qin, Elimination of zinc dendrites by graphene oxide electrolyte additive for zinc-ion batteries, ACS Appl. Energy Mater. 4 (2021) 4602–4609.
[31] A. Bayaguud, X. Luo, Y. Fu, C. Zhu, Cationic surfactant-type electrolyte additive enables three-dimensional dendrite-free zinc anode for stable zinc-ion batteries, ACS Energy Lett. 5 (2020) 3012–3020.
[32] W. Zhou, D. Zhu, J. He, J. Li, H. Chen, Y. Chen, D. Chao, A scalable top-down strategy toward practical metrics of Ni–Zn aqueous batteries with total energy densities of 165 W h kg^{-1} and 506 W h L^{-1}, Energy Environ. Sci. 13 (2020) 4157–4167.
[33] M. Song, H. Tan, D. Chao, H.J. Fan, Recent advances in Zn-ion batteries, Adv. Funct. Mater. 28 (41) (2018) 1802564.
[34] T. Zhang, Y. Tang, S. Guo, X. Cao, A. Pan, G. Fang, J. Zhou, S. Liang, Fundamentals and perspectives in developing zinc-ion battery electrolytes: a comprehensive review, Energy Environ. Sci. 13 (2020) 4625–4665.
[35] J. Hao, L. Yuan, B. Johannessen, Y. Zhu, Y. Jiao, C. Ye, F. Xie, S.Z. Qiao, Studying the conversion mechanism to broaden cathode options in aqueous zinc-ion batteries, Angew. Chem. Int. Ed. 60 (2021) 25114.
[36] T. Zhang, Y. Tang, G. Fang, C. Zhang, H. Zhang, X. Guo, X. Cao, J. Zhou, A. Pan, S. Liang, Electrochemical activation of manganese-based cathode in aqueous zinc-ion electrolyte, Adv. Funct. Mater. 30 (2020) 2002711.
[37] F. Crundwell, Analysis of the activation energy of dissolution of the iron-containing zinc sulfide (sphalerite), J. Phys. Chem. C 124 (2020) 15347–15354.
[38] F. Wang, E. Hu, W. Sun, T. Gao, X. Ji, X. Fan, F. Han, X.-Q. Yang, K. Xu, C. Wang, A rechargeable aqueous Zn^{2+}-battery with high power density and a long cycle-life, Energy Environ. Sci. 11 (2018) 3168–3175.
[39] S. Li, J. Fu, G. Miao, S. Wang, W. Zhao, Z. Wu, Y. Zhang, X. Yang, Toward planar and dendrite-free Zn electrodepositions by regulating Sn-crystal textured surface, Adv. Mater. 33 (2021) 2008424.
[40] M. Zhou, S. Guo, J. Li, X. Luo, Z. Liu, T. Zhang, X. Cao, M. Long, B. Lu, A. Pan, Surface-preferred crystal plane for a stable and reversible zinc anode, Adv. Mater. 33 (2021) 2100187.
[41] L. Hong, X. Wu, C. Ma, W. Huang, Y. Zhou, K.X. Wang, J.S. Chen, Boosting the Zn-ion transfer kinetics to stabilize the Zn metal interface for high-performance rechargeable Zn-ion batteries, J. Mater. Chem. A 9 (2021) 16814–16823.
[42] Q. Cao, H. Gao, Y. Gao, J. Yang, C. Li, J. Pu, J. Du, J. Yang, D. Cai, Z. Pan, Regulating dendrite-free zinc deposition by 3D zincopilic nitrogen-doped vertical graphene for high-performance flexible Zn-ion batteries, Adv. Funct. Mater. 31 (2021) 2103922.

[43] H. He, H. Zhang, D. Huang, W. Kuang, X. Li, J. Hao, Z. Guo, C. Zhang, Harnessing plasma-assisted doping engineering to stabilize metallic phase $MoSe_2$ for fast and durable sodium-ion storage, Adv. Mater. 34 (2022) 2200397.
[44] X. Li, S. Ling, W. Cao, L. Zeng, R. Yuan, C. Zhang, Surface-sdaptive capillarity enabling densified 3D printing for ultra-high areal and volumetric energy density supercapacitors, Angew. Chem. Int. Ed. 61 (2022) e202202663.
[45] X. Li, S. Ling, L. Zeng, H. He, X. Liu, C. Zhang, Directional freezing assisted 3D printing to solve a flexible battery dilemma: ultrahigh energy/power density and uncompromised mechanical compliance, Adv. Energy Mater. 12 (2022) 2200233.
[46] W. Sun, F. Wang, S. Hou, C. Yang, X. Fan, Z. Ma, T. Gao, F. Han, R. Hu, M. Zhu, Zn/MnO_2 battery chemistry with H^+ and Zn^{2+} coinsertion, J. Am. Chem. Soc. 139 (2017) 9775–9778.
[47] Y. Liu, H. He, A. Gao, J. Ling, F. Yi, J. Hao, Q. Li, D. Shu, Fundamental study on Zn corrosion and dendrite growth in gel electrolyte towards advanced wearable Zn-ion battery, Chem. Eng. J. 446 (2022) 137021.
[48] J. Shi, T. Sun, J. Bao, S. Zheng, H. Du, L. Li, X. Yuan, T. Ma, Z. Tao, Water-in-deep eutectic solvent" electrolytes for high-performance aqueous Zn-ion batteries, Adv. Funct. Mater. 31 (2021) 2102035.